Lee *et al. Nano Convergence* (2026) 13:15
https://doi.org/10.1186/s40580-026-00544-2

Nano Convergence

FULL PAPER Open Access

Resiquimod-loaded MOF525 enables synergistic photodynamic therapy and immunotherapy for colorectal cancer

Na Kyeong Lee[1,2†], Chi-Pin James Wang[1,2†], Soo-Hyun Lee[1], Nea Young Chun[3], Yu Jin Oh[3], Ulziituya Batjargal[4], Min-Seok Kim[4], WonJun Jang[4], Han-Jun Kim[4], Tae-Eun Park[5], Wooram Park[6,7*], Chun Gwon Park[1,2*] and Se-Na Kim[3,8*]

Abstract

Metal-organic frameworks (MOFs) represent a class of materials with exceptional potential for biomedical applications. In this study, a synergistic platform integrating photodynamic therapy (PDT) and immunotherapy was developed by loading the Toll-like receptor 7/8 agonist resiquimod (R848) into MOF525, a porphyrin-based metal–organic framework (R848@MOF525). Owing to the intrinsic photosensitizing properties of porphyrinic ligands and the high porosity of MOF525, R848@MOF525 was able to effectively generate reactive oxygen species upon 660 nm laser irradiation and sustainably release R848. In vitro studies using R848@MOF525 showed significant PDT-mediated cytotoxicity in colon adenocarcinoma cells (CT26) and increased extracellular release of adenosine triphosphate, indicating potential induction of immunogenic cell deaths. R848@MOF525 also strongly promoted dendritic cell maturation in vitro, further highlighting their potential roles as simultaneous immunostimulatory adjuvants. In a subcutaneous CT26 tumor-bearing mouse model, PDT using R848@MOF525 was able to yield faster tumor regression than with MOF525. Furthermore, tumor rechallenge tests also showed no evident tumor growth up to 3 weeks, indicating that PDT using R848@MOF525 could induce a durable systemic antitumor immunity. Notably, under an extended treatment interval, PDT mediated by MOF525 failed to suppress tumor growth, whereas PDT using R848@MOF525 successfully maintained antitumor efficacy. Collectively, these findings highlight R848@MOF525 as a promising platform for colorectal cancer treatment, synergistically employing immunotherapy to enhance the antitumor efficacy of PDT.

Keywords Colorectal cancer, Photodynamic therapy, Immunotherapy, Metal organic framework, Nanoplatform

†Na Kyeong Lee and Chi-Pin James Wang have contributed equally to this work.

*Correspondence:
Wooram Park
parkwr@skku.edu
Chun Gwon Park
chunpark@skku.edu
Se-Na Kim
snkim@mediark.kr

Full list of author information is available at the end of the article

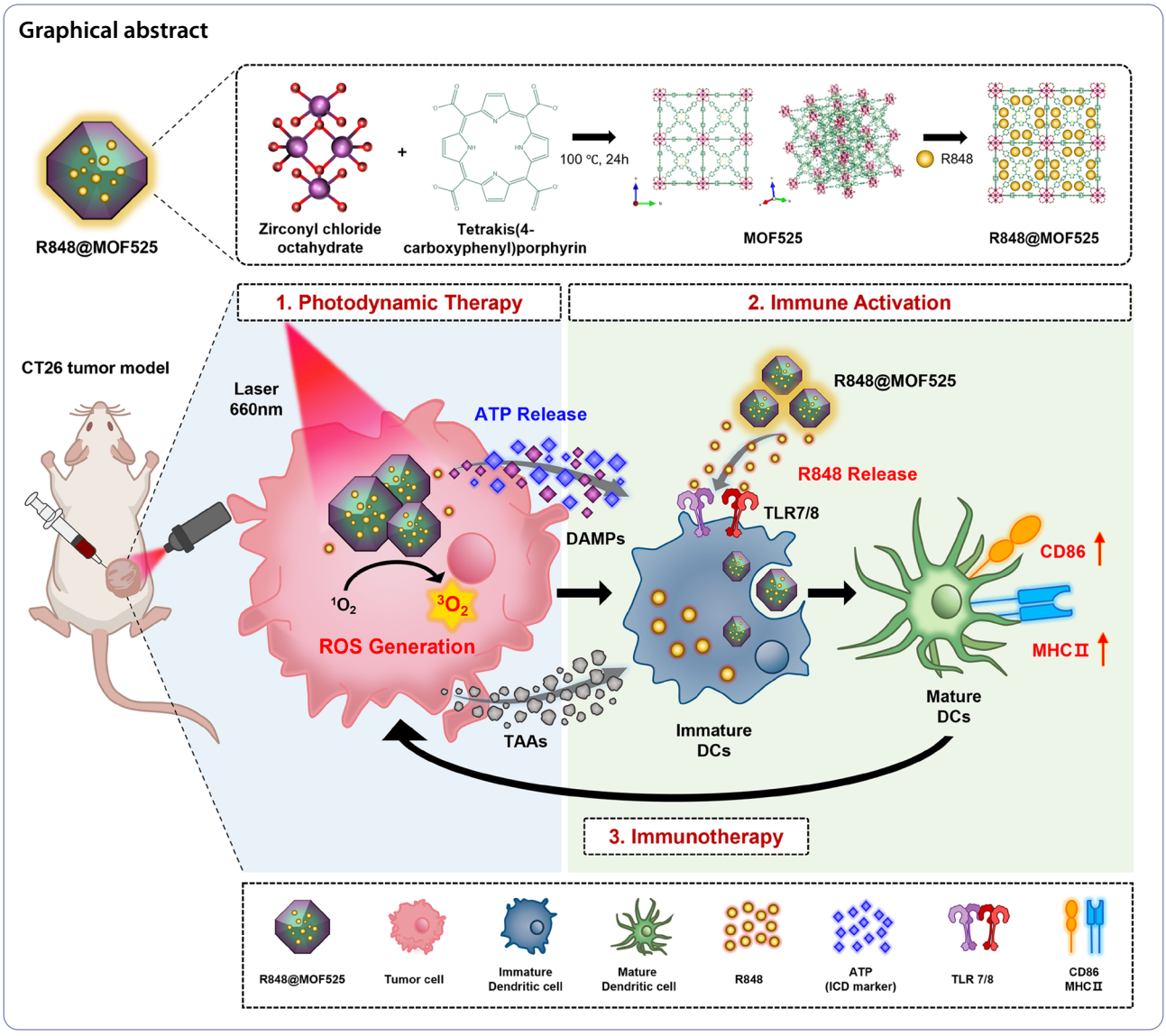

1 Introduction

Metal-Organic Frameworks (MOFs) have recently emerged as a promising class of materials with extensive applications across biomedical fields [1, 2] including cancer therapy [3–5]. MOFs are crystalline particles with highly ordered structures composed of metal ions coordinated to organic ligands [6–9]. The specific rotation angle and geometry that result from the interaction between metal ions and organic ligands lead to a range of distinct topologies [9–11]. Additionally, external factors such as reaction temperature, reaction duration, and reagent ratio also comprehensively contributes to the final morphology, making MOFs a structurally versatile platform [10, 12]. High porosity is another advantageous feature of MOFs that highlights their potential as therapeutic platforms, as the empty pores enable effective loading of therapeutic molecules [13–15]. Among various organic ligands, a unique group of ligands exhibit photoactive properties that can be utilized to develop photo-responsive MOFs [16, 17]. Porphyrin-based ligands, in particular, have drawn significant attention in phototherapy due to their ability to produce reactive oxygen species (ROS) in response to laser irradiation [18]. This unique property allows porphyrin-based MOFs to directly function not only as a drug delivery platform, but also as an effective ROS-producing photosensitizer [19].

Owing to the advantages of porphyrinic MOFs as both a drug delivery and a photodynamic therapy (PDT) platform, their roles are particularly prominent in colorectal cancer (CRC) treatment. CRC is an example of a cancer in which PDT offers great advantages over conventional therapies since PDT can be endoscopically delivered to lesions [20, 21] without an open surgery or other invasive approaches. PDT allows selective tumor ablation,

preserves adjacent healthy tissues, and enables repeated administration that underscores its significance against CRC [22, 23]. Unfortunately, despite localized tumor ablation, the efficacy of PDT is often limited by the immunosuppressive tumor microenvironment (TME) and tumor recurrence [20, 21]. To overcome this issue, numerous studies have attempted to combine PDT with other treatment modalities that can enhance its overall therapeutic efficacy [24, 25].

Resiquimod (R848) is a Toll-like receptor (TLR) agonist commonly used as an adjuvant in immunotherapy to activate innate immune cells and to promote adaptive immune responses [26–28]. By engaging TLR7/8 signaling, R848 induces dendritic cell (DC) maturation and bridges the innate and adaptive immunity against cancer [29–31]. Since R848 triggers immune responses that may overcome the immunosuppressive TME, its use in combination with PDT offers a promising strategy that can synergistically augment the therapeutic efficacy of traditional PDT [32–35]. Notably, tumor-associated antigens (TAAs) are critical components in adjuvant-mediated immunotherapy, as mature DCs utilize TAAs to orchestrate cancer-specific immune responses [36]. Consequently, immunotherapy is often suboptimal in poorly immunogenic tumors [37]. Considering that PDT can directly release immune-activating molecules such TAAs and danger-associated molecular patterns (DAMPs) via immunogenic cell death (ICD) [38], PDT may in turn also provide an immunologic environment favorable for the immune responses mediated by R848 [20, 39–42]. Combining PDT with R848 immunotherapy therefore offers several advantages compared to using each modality alone. Simultaneously employing both PDT and immunotherapy not only provides a more comprehensive approach to tumor eradication but also offers a promising strategy for synergistic cancer treatment.

Herein, this study reports the use of R848-loaded MOF525 (R848@MOF525) as a potential PDT platform against CRC. Among various porphyrin-based MOFs, MOF525 was selected for its high photo-reactivity and efficient ROS generation upon irradiation [3, 43–45]. MOF525 has also been reported to possess relatively higher surface area [46] suitable for greater drug loading, and greater singlet oxygen generation upon irradiation [47]. The high porosity of MOF525 enabled successful encapsulation of R848, which was sustainably released over a week in vitro. R848@MOF525 irradiated with 660 nm laser demonstrated high ROS generation and induction of ICD evaluated via ATP release in colon adenocarcinoma cells (CT26). Immunostimulatory properties assessed using bone marrow-derived dendritic cells (BMDCs) also revealed that R848@MOF525 and MOF525 both strongly promoted dendritic cell maturation in vitro, further highlighting their roles as immunostimulatory adjuvants. The therapeutic potential of R848@MOF525 was evaluated using a CT26 subcutaneous tumor model as illustrated in Scheme 1. When evaluated in vivo, PDT using R848@MOF525 was able to yield faster tumor regression than with MOF525. Furthermore, tumor rechallenge tests also showed no evident tumor growth up to 3 weeks, indicating that PDT using R848@MOF525 could induce a durable systemic antitumor immunity. Notably, under an extended treatment interval, PDT mediated by MOF525 failed to suppress tumor growth, whereas those using R848@MOF525 successfully maintained antitumor efficacy. This study collectively demonstrates that R848@MOF525 can significantly inhibit tumor growth and induce robust immune responses, highlighting its potential as a multifunctional therapeutic platform incorporating both PDT and immunotherapy.

Scheme 1.

2 Result and discussion

2.1 Characterization of MOF525 and R848@MOF525

In this study, MOF525, a porphyrin-based MOF, was developed as a photosensitizer and carrier of the immune adjuvant R848. MOF525, composed of zirconium (Zr) metal units and Tetrakis(4-carboxyphenyl)porphyrin (TCPP) organic ligands, was synthesized using a solvothermal method. Following MOF525 synthesis, R848 was loaded into the pores of MOF525 via immersion, resulting in the drug loaded R848@MOF525 (Fig. 1A). Scanning electron microscopy (SEM) images exhibited that fabricated MOF525 were cuboctahedral-shaped, as reported previously (Fig. 1B) [48]. SEM images further confirmed that this shape was not altered after R848 loading, although dynamic light scattering measurements showed a subtle increase in hydrodynamic diameter from 320.9 nm to 337 nm after loading R848 (Fig. 1B). The zeta potential of MOF525 or R848@MOF525 were each – 12.3 mV and – 9.5 mV, respectively (Fig. 1C). This slight increase in surface charge may be attributed to the loading of R848, as similarly observed in another study [49]. To determine the colloidal stability of MOF525 in a physiological condition, MOF525 was also dispersed in phosphate buffered saline (PBS) containing 5% (v/v) serum for five days. Both the hydrodynamic diameter and polydispersity index measurements remained stable up to three days, although these values slightly increased on Day 5 (Figure S1). These results demonstrate that MOF525 remains colloidally stable in physiologically relevant conditions without abrupt changes indicative of aggregation.

The fabricated MOFs showed a distinct X-ray diffraction (XRD) pattern unique to the structure and crystallinity of MOF525 reported previously (Fig. 1D) [50]. These XRD patterns were similarly maintained with R848@MOF525, indicating that R848 loading did not

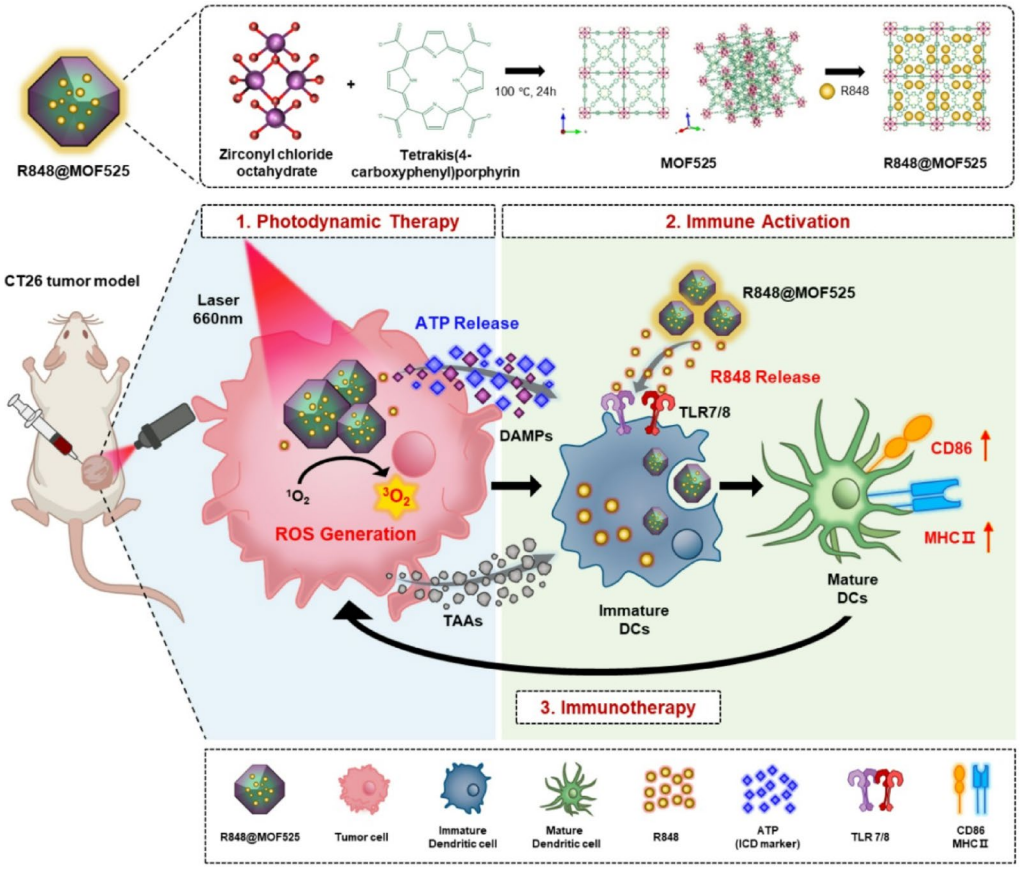

Scheme 1 Schematic diagram illustrating the fabrication process of R848@MOF525 and the therapeutic mechanism behind how R848@MOF525 synergistically employs immunotherapy to enhance the antitumor efficacy of PDT. Created using BioRender.com

significantly alter the unique crystallinity of MOF525 (Fig. 1D). Next, N_2 adsorption-desorption isotherms of MOF525 and R848@MOF525 were evaluated. The isotherm graphs of MOF525 showed a dominant presence of micropores whereas these were reduced after loading R848 (Fig. 1E). The Brunauer-Emmett-Teller (BET) specific surface area and Barrett-Joyner-Halenda (BJH) specific pore volume of MOF525 was each 1356 $m^2\ g^{-1}$and 0.8044 $cm^3\ g^{-1}$, respectively (Table S1). Incorporating R848 caused these values to each decrease to 80.18 $m^2\ g^{-1}$ and 0.5597 $cm^2\ g^{-1}$, confirming successful loading of R848 within MOF525. Although the average pore diameter of R848@MOF525 increased from 1.682 nm to 66.93 nm, such change does not necessarily indicate a structural expansion, but is rather likely due to the shift in pore distribution as shown in Fig. 1E.

Fourier transform infrared spectroscopy (FTIR) analysis of MOF525 showed distinct peaks at 1600 cm^{-1} (asymmetric stretching of carboxylate ligand), 1410 cm^{-1} (symmetric stretching of carboxylate ligand), and 660 cm^{-1} (stretching mode of the metal-ligand bonds) indicative of Zr-porphyrin MOFs [51] (Fig. 1F). These characteristic peaks were also observed in R848@MOF525, with additional peaks emerging at 3112 cm^{-1} (stretching vibration of = C-H bonds) and 2975 cm^{-1} (stretching of -C-H bonds), which were attributable to R848. To further examine whether any chemical interactions were present between R848 and MOF525, X-ray photoelectron spectroscopy (XPS) analysis was performed in the Zr 3d region before and after R848 loading (Fig. 1G). MOF525 alone displayed characteristic peaks corresponding to the Zr–O coordination [52]. Interestingly, a new signal emerged following R848 loading, which was attributable to O–Zr–N bonding. These results suggest that the Lewis basic nitrogen atoms of R848 may have formed coordination bonds with unsaturated Lewis acidic Zr^{4+} centers within the MOF525 framework [53]. Considering that such interactions are reversible under aqueous or physiological conditions, the presence of coordination bonds between R848 and surface Zr sites presents an interaction suitable for in vivo drug release [54].

2.2 In vitro evaluation of antitumor efficacy

The release profile of R848 from R848@MOF525 was analyzed using a dialysis-based method by suspending the MOFs in pH 7.4 PBS under mild shaking. The drug loading capacity of R848@MOF525 was determined as

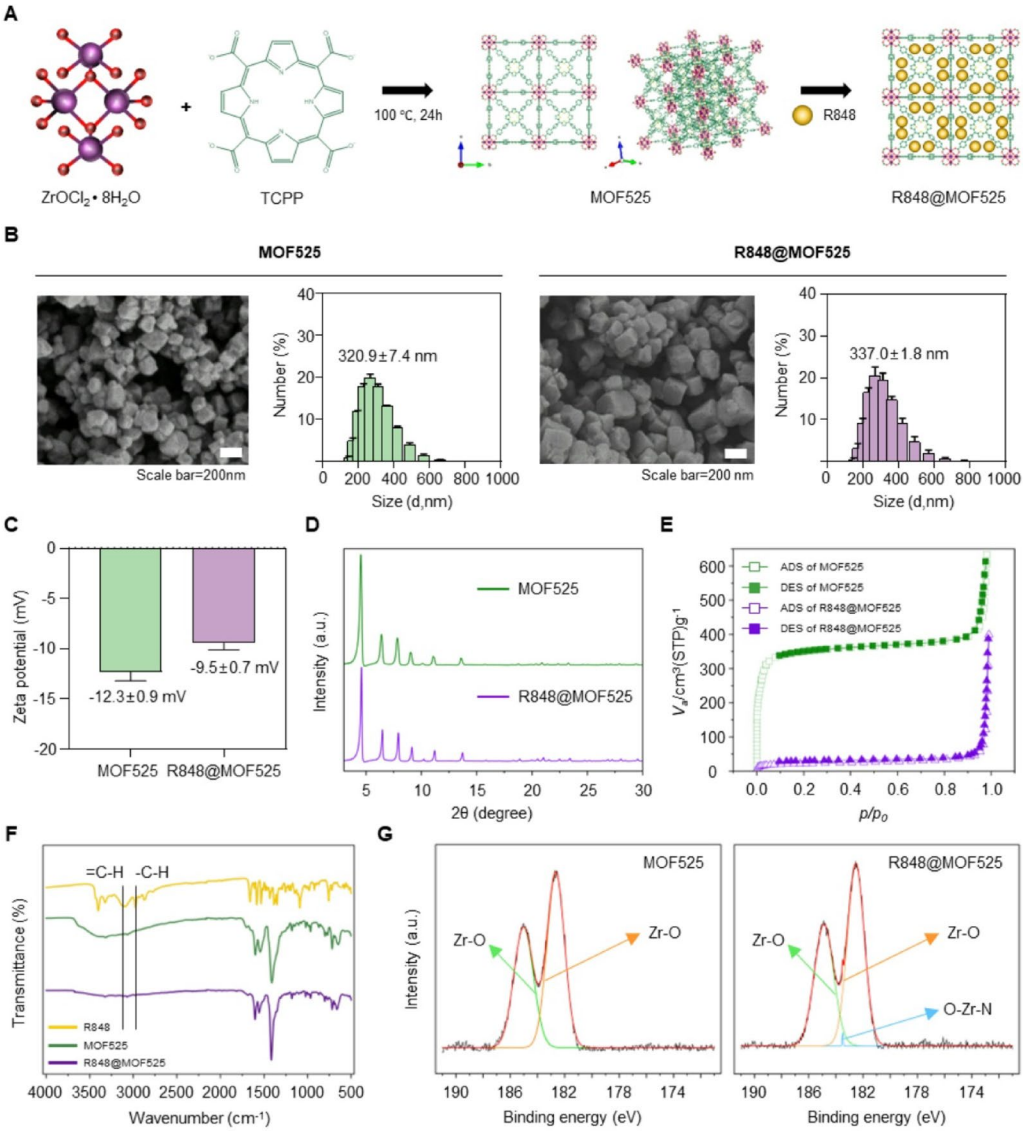

Fig. 1 Characterization of MOF525 and R848@MOF525. **A** Schematic diagram illustrating the fabrication process of MOF525 and R848@MOF525. **B** SEM images and size distribution histograms of hydrodynamic diameters. **C** Zeta potential measurements. **D** Powder XRD patterns. **E** N_2 adsorption-desorption isotherms. **F** FTIR spectra **G** XPS spectra in the Zr 3d region of (left) MOF525 and (right) R848@MOF525. Data presented as mean ± standard deviation

approximately 44 μg R848 per 1 mg MOF via reverse phase high-performance liquid chromatography (HPLC). The drug release profile was observed over 12 days, revealing that the majority of the payload was sustainably released until Day 7 (Fig. 2A). Cell cytotoxicity of MOF525 and R848@MOF525 was assessed in vitro using L929 mouse fibroblast cells as recommended by ISO 10993-5 [55]. According to the ISO 10993-5:2009 guideline, MOF concentrations exhibiting cell viability greater than 70% compared to negative control was considered as non-toxic [56]. Both MOF525 and R848@MOF525 showed a dose-dependent cytotoxicity toward L929 (Fig. 2B) but were not toxic below 50 μg/mL. Subsequently, MOF concentration of 50 μg/mL was chosen for further in vitro and in vivo experiments.

To examine whether the porphyrin ligands of MOF525 or R848@MOF525 could generate ROS in response to laser irradiation, ROS production was quantified in vitro using the singlet oxygen sensor green (SOSG) assay. When MOFs were irradiated using a 660 nm laser (500 mW) up to 10 min, SOSG intensities of both MOF525 and R848@MOF525 showed a gradual increase, indicating effective ROS generation (Fig. 2C). In terms of signal intensity, the SOSG signal produced by R848@MOF525 was weaker than those of MOF525. However, this is likely due to the absolute difference in the amount of porphyrin ligands present in each group. Due to the increased mass following encapsulation of R848, identical weights of MOF525 and R848@MOF525 could have resulted in differing amount of porphyrin ligands. Nevertheless,

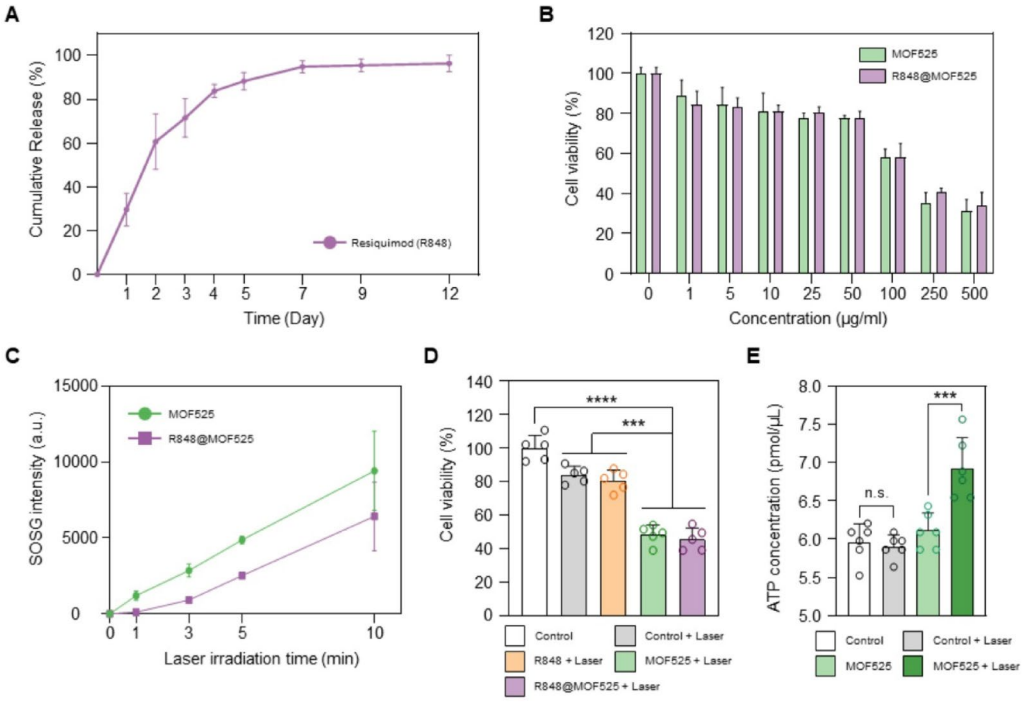

Fig. 2 In vitro evaluation of the photodynamic and anticancer efficacy of MOF525 and R848@MOF525. **A** R848 release profiles over 12 days ($n=3$). **B** Viability of L929 cells exposed to varying concentrations of MOFs ($n=6$). **C** ROS generation induced by MOF525 and R848@MOF525 ($n=3$). **D** PDT effect of MOF525 on CT26 cells ($n=5$, $^{****}P<0.0001$, $^{***}P<0.0002$). **E** Quantification of extracellular ATP release following different treatments ($n=5$, $^{***}P<0.002$). Data presented as mean ± standard deviation

R848@MOF525 also exhibited notable ROS production following irradiation, confirming its potential as a PDT platform.

Next, the anticancer efficacy of PDT using R848@MOF525 was evaluated against CT26 colon adenocarcinoma cells. The viability of CT26 cells treated with either MOF525 + Laser or R848@MOF525 + Laser were significantly reduced compared to non-treated control (Fig. 2D). Although cells treated with laser alone also exhibited a subtle decrease in cell viability, PDT mediated by MOF525 showed significantly amplified anticancer effects, presumably due to ROS generation. These findings suggest that MOF525 effectively functions as cytotoxic photosensitizers upon laser irradiation. To further evaluate whether PDT mediated by MOF525 could induce sufficient immunogenic cell death in tumor cells, extracellular adenosine triphosphate (ATP), a representative damage-associated molecular patterns (DAMP) marker, was quantified following PDT. Among treatment groups, MOF525 treatment with laser irradiation induced significantly greater ATP release (6.92 pmol/μL) compared to MOF525 treatment alone (6.11 pmol/μL) or control (5.96 pmol/μL) (Fig. 2E). Despite the slight reduction in CT26 viability (Fig. 2D), laser treatment alone induced ATP releases comparable to those of untreated control. To further assess potential thermal effects associated with laser irradiation, the photothermal characteristics of MOF525 were evaluated. Upon irradiation with a 660 nm laser (500mW) for 5 min, MOF525 exhibited a temperature increase of approximately 3.4 °C (Figure S2). Although this increase was greater than those observed for PBS, both the endpoint (28.9 °C) and change (3.4 °C) in temperature was substantially lower than those typically required for photothermal therapy or tumor ablation [57, 58]. *While potential immunogenic contributions of mild hyperthermia cannot be completely excluded* [59], its specific contribution to the overall therapeutic effect, particularly in relation to PDT, remains to be further elucidated.

In addition to the photodynamic properties of R848@MOF525, its potential as a synergistic immunotherapy platform was also evaluated in BMDCs using DC maturation markers as an indication of immune activation. To assess DC maturation induced by MOF525 and R848@MOF525, different concentrations of MOFs were co-incubated with BMDCs and analyzed for changes in surface CD86 and MHCII expression using flow cytometry (Fig. 3A). Here, CD86 and MHCII were selected as model indicators of immune stimulation as mature DCs present up-regulated expression of surface costimulatory molecules such as CD86 and MHCII compared to immature DCs [60–62]. The flow cytometry gating used to specify BMDCs is depicted in Figure S3. The expression of CD86 and MHCII induced by R848@MOF525 treatment were

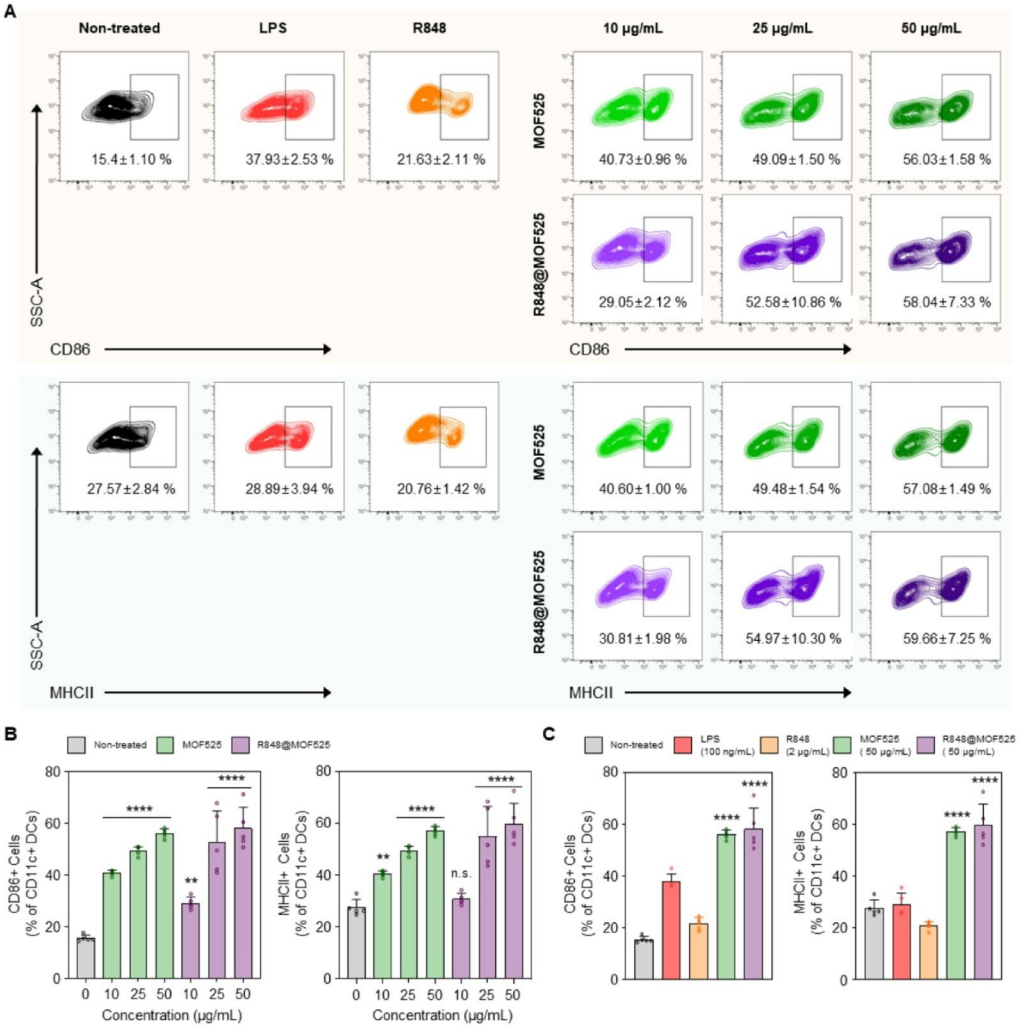

Fig. 3 Flow cytometry analysis of BMDC maturation induced by MOF525 and R848@MOF525 in vitro. Representative flow cytometry plots of the expression of **A** CD86 and MHCII exposed to various treatments ($n=5$). **B** CD86 and MHCII expression levels of BMDCs treated with various concentrations of MOF525 or R848@MOF525 ($n=5$, $^{****}P<0.0001$, $^{**}P<0.0021$ compared to the non-treated group). **C** CD86 and MHCII expressions induced in BMDCs treated with 50 μg/mL MOFs compared to either LPS or R848 ($n=5$, $^{****}P<0.0001$ compared to the LPS-treated group) Data presented as mean ± standard deviation

both significantly greater than those of the non-treated group, successfully demonstrating a dose-dependent immunostimulatory profile of MOFs (Fig. 3B). Although BMDCs treated with R848@MOF at concentrations below 10 μg/mL also exhibited a subtle increase in CD86 and MHCII expression, the changes were less significant than BMDCs treated with higher MOF concentrations (Figure S4).

Interestingly, the data also revealed that even MOF525 treatment alone was able to induce a notable change in both DC maturation markers without the adjuvant R848, suggesting a possible synergistic role of MOF525 as a self-standing immunostimulatory adjuvant. The specific mechanism behind the immunostimulatory properties of MOF525 have not yet been addressed, but this effect may have arisen from the adjuvant-like property of zirconium. Zr^{4+} ion is known to stimulate innate immune responses and promote DC maturation [63] while other studies have reported the potential role of zirconium salts as adjuvant-like materials via complement activation [64] or IgM antibody production [65]. As zirconium oxides have also been investigated as mild adjuvants [66], various active forms of zirconium released from MOF525 may have induced the observed changes in DC maturation markers. The expression of CD86 in BMDCs treated with either 50 μg/mL MOF525 (56.03 ± 1.58%) or R848@MOF525 (58.04 ± 7.33%) was both elevated by more than 3.6 folds compared to non-treated control (15.4 ± 1.10%). Similarly, the expression of MHCII in BMDCs treated with either 50 μg/mL MOF525 (57.08 ± 1.49%) or R848@MOF525 (59.66 ± 7.25%) was also over 2 folds greater than those of non-treated control (27.57 ± 2.84%) (Fig.

3C). These immunostimulatory effects were also notably greater when compared to BMDCs treated with free R848 (CD86: 21.63 ± 2.11%; MHCII: 20.76 ± 1.42%) or lipopolysaccharide (CD86: 37.93 ± 2.53%; MHCII: 28.89 ± 3.94%).

Another notable observation was that the expression of DC maturation markers in cells treated with either MOF525 or R848@MOF525 was comparable, which did not clearly delineate the additional contribution of the loaded drug. Although DCs treated with R848@MOF525 exhibited higher expression levels of CD86 and MHCII compared to those treated with MOF525 alone, these differences were not statistically significant. This observed phenomenon may be attributed to the release profile of R848 (Fig. 2A). Considering the 24 h treatment duration used in this in vitro study, the amount of R848 released during this period can be estimated to be approximately 0.66 μg/mL. While 2 μg/mL of free R848 was included as a positive control resembling the total R848 content within R848@MOF525, free R848 treatment also did not induce significant changes in expression of CD86 or MHCII (Fig. 3C). Despite the well-established role of R848 as a TLR7/8 agonist and its efficacy in cancer immunotherapy [67], several studies have also similarly reported limited changes in CD86 expression following R848 treatment in myeloid DCs and BMDCs under in vitro conditions [68, 69]. Collectively, the observed increase in CD86 and MHCII expression following treatment with either MOF525 or R848@MOF525 suggest that these MOFs possess inherent immunostimulatory properties. At the same time, these findings denotes the possibility of in vitro assays not fully depicting the immunotherapeutic contribution of R848, necessitating further in vivo evaluations to comprehensively assess its contributory role in this study.

2.3 In vivo evaluation of antitumor efficacy

The antitumor efficacy of R848@MOF525 was further verified in vivo using a subcutaneous colon carcinoma model. Mice were subcutaneously inoculated with CT26 colon adenocarcinoma cells, then subjected to various treatments (PBS; R848; MOF525; R848@MOF525; MOF525 + Laser; R8482MOF525 + Laser) once tumors reached an average volume of approximately 100 mm^3 (Fig. 4A). Treatment groups without laser irradiation were intratumorally injected with appropriate solutions while PDT groups received additional irradiation using a 660 nm laser (500 mW) for a total duration of 10 min. To induce PDT while avoiding localized heating, laser irradiation was divided into two 5 min treatments.

As depicted in Fig. 4B, treatment of either MOF525 or R848 alone was not able to induce significant regressions in tumor size. Interestingly, despite comparable immunostimulant properties between MOF525 and R848@MOF525 in vitro (Fig. 3C), the presence of R848 was able to elicit significantly greater tumor regressions in vivo, presumably owing to the sustained release of R848 (Fig. 4B-D). In groups that received PDT, both MOF525 + Laser and R848@MOF525 + Laser treatments demonstrated significant anti-tumor effects, inducing complete tumor regression by Day 40 (Fig. 4C). Such results highlight the significance of porphyrin-based MOF525 as an effective platform for PDT against tumors. However, in terms of tumor regression rates, R848@MOF525 combined with PDT was able to induce a more rapid regression, as all treated mice exhibited complete tumor regression even before Day 25 (Fig. 4B). In PDT groups that were treated with MOF525, complete tumor regression across all mice was observed on Day 35 without any significant changes in body weight (Fig. 4E). To investigate whether treatment of R848@MOF525 combined with PDT may also induce long-term immunity, mice that exhibited complete tumor regression were re-challenged with CT26 cells on the opposite flank on Day 60. Considering the growth rate of CT26 tumors observed after primary inoculation (Fig. 4B) and monitoring periods previously reported in similar studies [70–72], tumor growth was monitored for 3 weeks following re-challenge. Even after 3 weeks, no signs of tumor growth or nodule formation was observed in the re-challenged site, indicating that the initial PDT treatment not only ablates the primary tumor, but may also establish a robust systemic immune response (Figure S5).

To further validate the synergistic contribution of R848, an additional in vivo study was performed employing an extended treatment interval (Figure S6). The treatment interval was extended from the original 3 to 5 days to evaluate whether PDT using MOF525 or R848@MOF525 could also induce sufficient tumor regression with less frequent treatments. Unlike the results from treatments using a 3-day interval (Fig. 4B), PDT treatments using MOF525 was not able to induce tumor regression under the 5-day treatment interval, suggesting that the current treatment interval was insufficient to overcome the immunosuppressive TME (Fig. 4F, S7). On the contrary, mice treated with PDT using R848@MOF525 showed significantly greater tumor regression, particularly after the third treatment. These findings across different treatment schedules collectively suggest that although the antitumor effects of PDT cannot be overlooked, delivery of R848 via R848@MOF525 can significantly accelerate tumor regression and allow suboptimal PDT treatments to overcome the immunosuppressive TME. Such results suggests that PDT using R848@MOF525 may offer therapeutic advantages over MOF525 in tumors with higher proliferation rates or stronger immunosuppressive environments. Under these circumstances, R848@MOF525 presents a promising platform that can synergistically

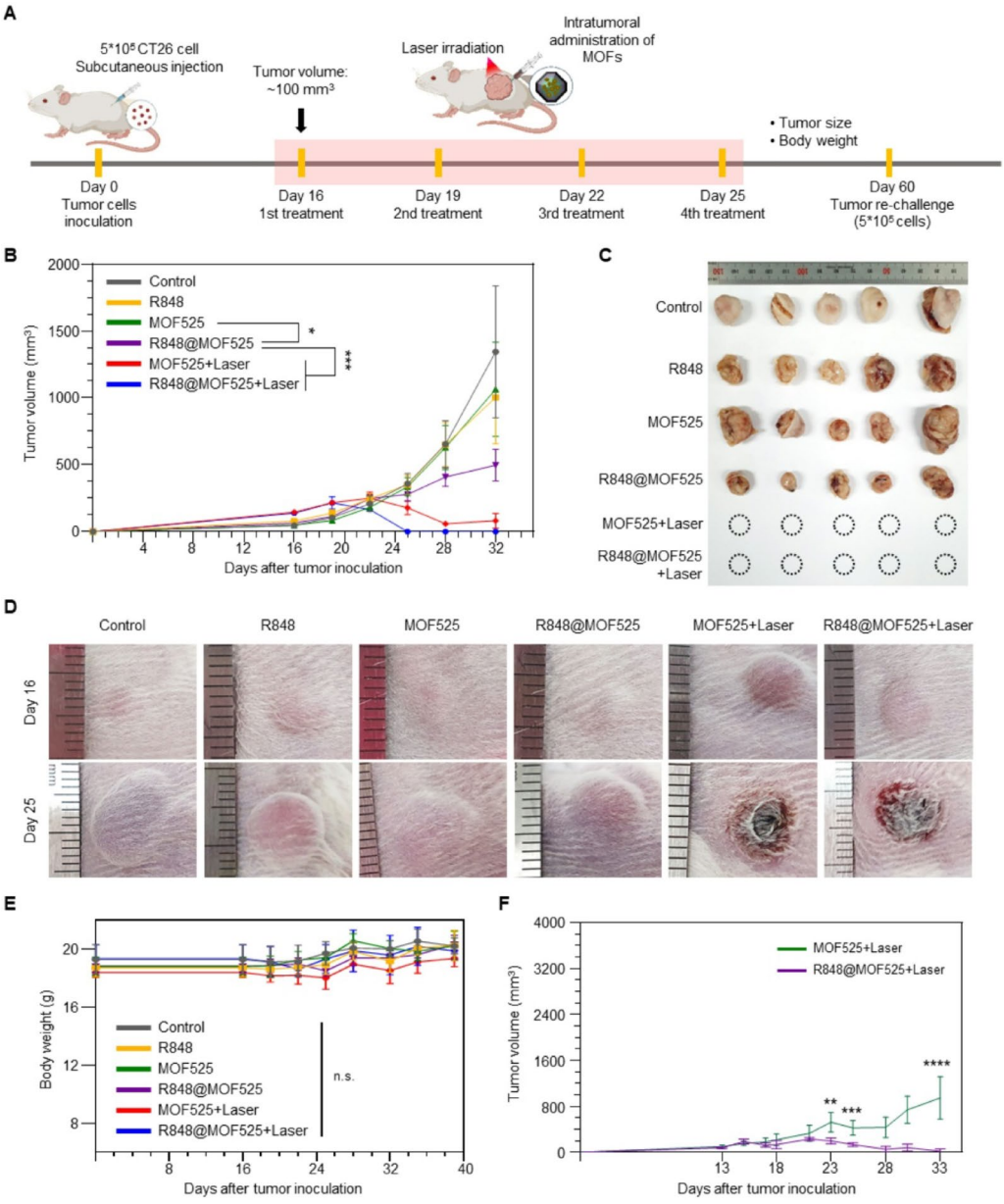

Fig. 4 In vivo antitumor efficacy of MOF525 and R848@MOF525 treatment under laser irradiation. **A** Schematic diagram of the CT26 subcutaneous tumor model and subsequent treatment schedules used in this study. **B** Tumor growth curves following various treatments ($n = 5$, $^{*}P < 0.0332$, $^{***}P < 0.0002$). **C** Photographic images of excised tumors collected from each group at 40 days after tumor inoculation. **D** Representative photographs of tumor sites before first and final (fourth) treatment. **E** Body weight changes of treated mice across 40 days ($n = 5$). **F** Average growth curves of tumors that received PDT treatments under a 5-day treatment interval ($n = 4$, $^{**}P < 0.0021$, $^{***}P < 0.0002$, $^{****}P < 0.0001$). Data presented as mean ± standard error of the mean

amplify the therapeutic efficacy of porphyrin-based MOFs used in PDT.

2.4 Histopathologic evaluation of antitumor efficacy

As PDT-treated mice exhibited complete tumor regression (Fig. 4B), histopathological analyses were not conducted in these groups. Instead, tumors remaining in mice treated with either PBS, R848, MOF525 or R848@MOF525 were collected and fixed in 10% neutralized buffered formalin for histopathological evaluations. Tumor samples were subjected to a general paraffin embedding procedure, followed by hematoxylin and eosin (H&E) staining. To assess the overall size and cellular composition of the tumor, whole mount image was collected (Fig. 5A). Remaining tumors, in terms of area, were found to be larger in the order of control, MOF525, R848, and R848@MOF525 groups (Fig. 5A, B). Necrotic lesions were present in the central area of all treatment groups, although tumors treated with MOF525 had a wider necrotic lesion compared to those treated

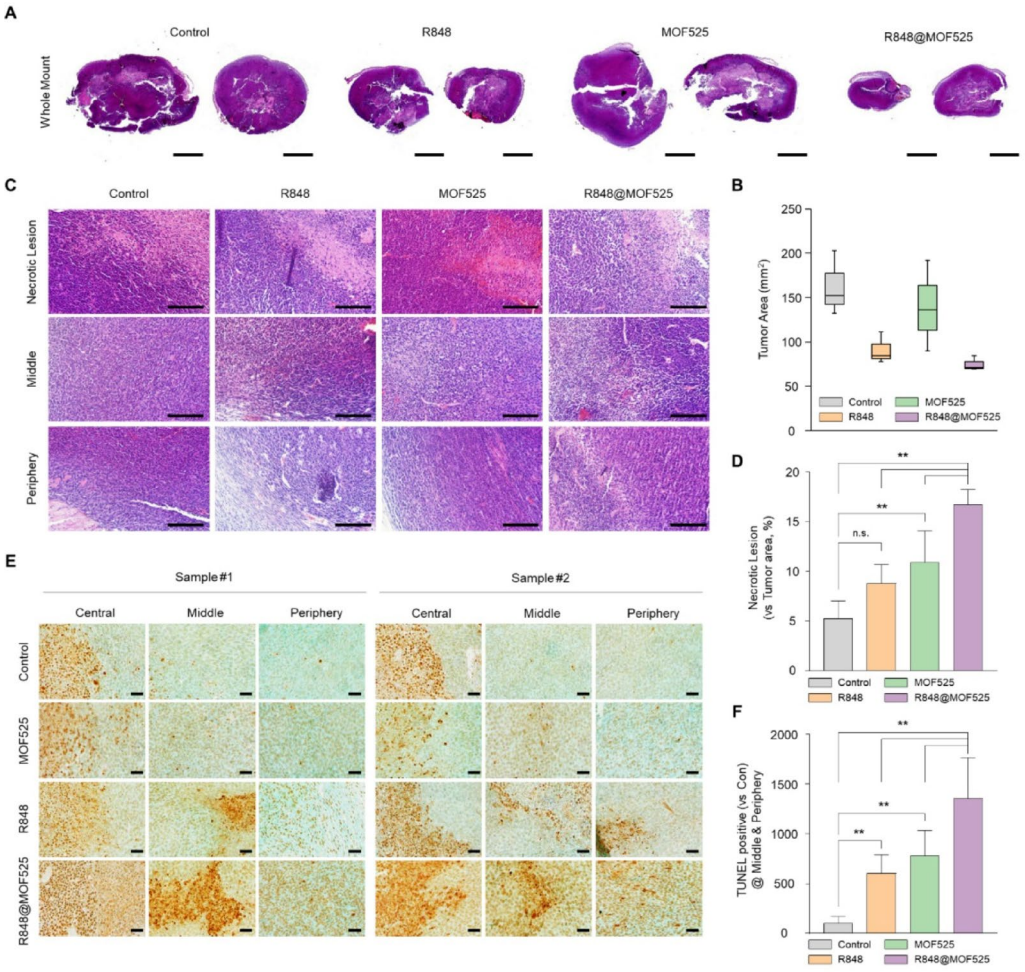

Fig. 5 Histopathological analysis of CT26 tumors treated with R848@MOF525. **A** Representative whole-mount tumor images. Scale bar: 2 mm. **B** Quantitative analysis of microscopic tumor areas. **C** H&E stained tumor Sect. (200 × magnification) showing central necrosis, inflammatory infiltration (middle), and active tumor proliferation (periphery). Scale bar: 100 μm. **D** Quantitative analysis of necrotic lesions in tumor areas across experimental groups. ($n = 5$, $^{*}P < 0.0332$, $^{**}P < 0.0021$) **E** Representative TUNEL staining images across central, middle, and peripheral regions. Scale bar: 50 μm. **F** Quantification of TUNEL-positive cells ($n = 3$, $^{**}P < 0.0021$). Data presented as mean ± standard deviation

with R848. The size of tumors treated with R848@MOF525 was smaller overall, with smaller foci of necrosis found throughout the tumors in addition to the central necrotic lesions.

When observed at a higher magnification, necrotic lesions composed of amorphous necrotic material were observed in all groups, with a large number of inflammatory cells infiltrating around these necrotic lesions (Fig. 5C). Furthermore, while the inflammatory cell infiltration was not prominent in the proliferating region of tumor in the control group, tumors from other treatment groups (R848, MOF525, and R848@MOF525) had varying degrees of inflammatory cell infiltration. Tumors treated with R848@MOF525, in particular, showed the formation of small necrotic foci with scattered inflammatory cell infiltration. Compared to tumors treated with MOF525, more mononuclear cell infiltration was observed in the middle and periphery lesion of those treated with R848. Quantitative analysis of necrotic lesions further showed that the relative necrotic lesion (necrotic lesion: tumor area) of tumors treated with either MOF525 or R848@MOF525 was both significantly greater than those of the control group (Fig. 5D). No statistical significance was observed between tumors treated with either MOF525 or R848. Among experimental groups, tumors treated with R848@MOF525 had the largest relative necrotic lesions, although this may be due to their relatively smaller tumor size as well as the inclusion of both central and sporadic necrotic lesions, collectively leading to an increase in relative necrotic foci.

Furthermore, TUNEL staining was performed to evaluate the extent of apoptotic cell death in the tumor. Central necrosis was observed in all groups, characterized by the presence of multiple TUNEL positive cells (Orange to brownish color) (Fig. 5E). In particular, multiple TUNEL positive apoptotic cell death foci in the area between

the central necrosis and the periphery was observed in tumors treated with either R848 or R848@MOF525. Quantitative analysis also showed that the TUNEL positive areas of tumors treated with R848@MOF525 were significantly higher than all other treatment groups (Fig. 5F). Taken together, these histopathological analyses indicate that although R848@MOF525 treatment did not yield complete tumor regression, R848 released from R848@MOF525 was still able to induce stronger necrosis, apoptotic cell death, and infiltration of inflammatory cells in tumors compared to those treated with bare MOF525.

2.5 In vivo biosafety evaluation

The systemic toxicity of R848@MOF525-mediated PDT therapy was evaluated by conducting a toxico-pathological analysis across major vital organs (e.g. Heart, Lung, Liver, Kidney, Spleen) harvested 3 weeks after the tumor rechallenge test (Figure S8). Following PDT treatment using either MOF525 or R848@MOF525, a mild proliferation of pulmonary interstitial tissue, a mild increase in the number of reactive hepatocytes in the liver, and a mild increase in the size of splenic nodules were observed in some individual specimens. However, these changes were likely mild side effects of immunologic responses to the repetitive tumor inoculations and subsequent tumor cell therapies. No significant damage to vital organs were observed in any of the evaluated mice. These results confirm that PDT utilizing R848@MOF525 exerts no systemic toxicity.

3 Conclusion

In this study, a porphyrin-based metal–organic framework platform loaded with R848, namely R848@MOF525, was fabricated to integrate PDT with immunotherapy for colorectal cancer treatment. MOF525, the parent of R848@MOF525, provided a highly porous structure capable of efficiently encapsulating the Toll-like receptor agonist R848 while simultaneously functioning as a photosensitizer owing to the presence of porphyrin ligands. Structural and spectroscopic analyses confirmed that R848 loading did not alter the crystallinity nor the morphology of MOF525, and drug release studies demonstrated sustained release of R848 up to seven days. In vitro experiments showed that R848@MOF525 effectively generated ROS under 660 nm laser irradiation, leading to PDT-like cytotoxic effects in CT26 colon adenocarcinoma cells and inducing immunogenic cell death, as evidenced by increased extracellular ATP release. Furthermore, MOF525 and R848@MOF525 were both able to promote notable DC maturation as indicated by elevated expression of CD86 and MHCII in BMDCs, suggesting that MOF525 itself could also stimulate immune activation in addition to mediating PDT.

The therapeutic potential of R848@MOF525 was further validated in vivo using a CT26 tumor-bearing mouse model. While MOF525-mediated PDT alone also effectively suppressed tumor growth, the incorporation of R848 significantly accelerated tumor regression and demonstrated persistent antitumor effects even under extended treatment intervals. Notably, mice that achieved complete tumor regression following R848@MOF525-mediated PDT showed no tumor growth in tumor rechallenge tests, indicating that R848@MOF525-mediated PDT could induce a durable systemic antitumor immunity. Histopathological analyses further supported these findings by revealing enhanced necrosis, apoptosis, and inflammatory cell infiltration in tumors treated with R848@MOF525. While the present study demonstrates promising therapeutic efficacy and suggests the induction of antitumor responses, further in vivo immunological characterization could enhance mechanistic understanding. In particular, comprehensive temporal evaluation of tumor-infiltrating lymphocytes may delineate the immunological mechanisms underlying therapeutic efficacy, as well as to further elucidate the immunological impact of prolonged R848 release. Such investigations represent a valuable direction for future studies. Nevertheless, these results collectively demonstrate that R848@MOF525 represents a promising photoimmunotherapeutic platform capable of synergistically enhancing PDT efficacy and overcoming immunosuppressive tumor environments via immunotherapy.

4 Materials and methods

4.1 Materials

Benzoic acid (assay ≥ 99.0%), TCPP (assay ≥ 97.0%) and R848 (assay ≥ 98.0%) were purchased from TCI (Japan). Dimethylformamide (DMF, assay ≥ 99.5%) was purchased from DAEJUNG (Korea). Zirconyl chloride octahydrate ($ZrOCl_2$ $8H_2O$) and LPS from *E. coli* (O55:B5) were purchased from Sigma-Aldrich (USA). Dulbecco's Modified Eagle Medium (DMEM), RPMI 1640 Medium (RPMI) and Phosphate buffered saline (pH 7.4) were purchased from Thermo Fisher Scientific (USA).

4.2 Preparation of MOFs

MOF525 was synthesized following a previously reported protocol with slight modifications [73]. Briefly, TCPP (235 mg, 0.297 mmol) and benzoic acid (6750 mg, 55 mmol) were dissolved in 40 mL DMF and sonicated for 30 min. $ZrOCl_2$ $8H_2O$ (525 mg, 1.62 mmol) was added to the TCPP solution and subsequently dissolved for 30 min. The resulting solution was heated in an oven at 100 ℃ for 24 h. The resultant products were collected by centrifugation and washed thrice with DMF and ethanol to remove excess reactants. The resulting particles were dried at 80 ℃ for 6 h to achieve dry powders.

Subsequently, MOF525 was dried under vacuum at 150 ℃ to clear the pores and remove residual solvent. To prepare R848@MOF525, 20 mg R848 was first dissolved in 2 mL ethanol and sonicated, to which 100 mg of activated MOF525 were added. The suspension was kept at RT for 24 h. Then, R848-loaded MOF525 was filtered using a 200 nm PVDF membrane filter, washed with ethanol thrice, and dried at 70 ℃ to achieve R848@MOF525.

4.3 Characterizations

Images of the morphology and size of MOF525 and R848@MOF525 were obtained using a SEM (Dimension ICON, Bruker, USA). The hydrodynamic size and zeta potential were measured using a Zetasizer (Zetasizer pro, Malvern Panalytical, UK) while the serum stability of MOFs were evaluated after incubation in PBS containing 5% FBS. PXRD patterns were recorded using an X-ray diffractometer (SmartLab, Rigaku, Japan) at 3 kW with CuKα radiation. A surface area and porosity analyzer (Autosorb IQ, Quanmtachrome, USA) at -196℃ was used to measure the surface area, pore size, and pore volume of MOFs. FTIR spectra of MOF525 and R848@MOF525 were analyzed using a FTIR spectrophotometer (Cary670 (Main bench) + Cary620 (microsocope)), Agilent, USA) over the range from 4000 to 500 cm^{-1} at room temperature. The XPS spectra of MOF525 and R848@MOF525 were obtained using an X-Ray Photoelectron Spectroscopy System (PHI Quantera-Ⅱ, Ulvac-PHI, Japan).

4.4 R848 release profile in vitro

The release profile of R848 form R848@MOF525 was evaluated using a dialysis-based method. 5 mg of R848@MOF525 was dispersed in 5 mL of PBS and placed in the inner compartment of the SnakeSkin® dialysis tubing (MWCO: 3500, Thermo Fisher Scienticfic, USA). The tube was dialyzed against 20 mL of the same buffer at 37 ℃ under mild shaking. At each predetermined time points, the outer solution was recovered and replaced with equivalent volume of fresh PBS. The obtained samples were centrifuged at 17,000 rpm for 10 min and the supernatant was used for subsequent analyses. R848 content of the supernatant samples was quantified using reverse phase high-performance liquid chromatography (1260 Infinity Ⅱ, Agilent, USA). The mobile phase consisted of 60% 20 mM PBS containing phosphoric acid (pH 2.5) and 40% acetonitrile, with a flow rate of 1.0 mL/min. R848 was detected at 249 nm, with the injection volume of 10 μL. Maximum R848 loading was separately quantified by dispersing R848@MOF525 in PBS at a concentration of 0.5 mg/mL and sonicating for 3 h to fully extract the encapsulated drug.

4.5 Cell culture

L929 mouse fibroblast cells were cultured with DMEM containing 10% (v/v) fetal bovine serum (FBS) and 1% (v/v) Penicillin-Streptomycin (Gibco, Life Technologies, USA) in a cell incubator (5% CO_2, 37 °C). CT26 mouse colon cancer cells (ATCC, USA) were cultured with RPMI containing 10% (v/v) FBS and 1% (v/v) Penicillin-Streptomycin in a cell incubator (5% CO_2, 37 °C).

4.6 Cytotoxicity evaluation in vitro

Cytotoxicity of MOF525 and R848@MOF525 was evaluated in vitro using a water-soluble tetrazolium salt-based cell viability assay (EZ-Cytox; Daeil Lab Service, Korea) against L929 cells. L929 cells were seeded at a density of 0.9×10^4 cells/well in a 96-well cell culture plate and incubated for 24 h to ensure complete cell attachment. Next, the medium was completely removed and replaced with fresh medium containing either MOF525 or R848@MOF525 at varying concentrations (50, 25, 10 and 1 μg/mL) and incubated for another 24 h. Cells were washed thrice with PBS, then incubated for 1 h in 10% (v/v) EZ-Cytox solution diluted in medium. The absorbance at 450 nm was measured with a reference wavelength at 600 nm using a microplate reader (Synergy H1, BioTek, USA). Cell viability was calculated by using the following equation:

$$Cell\ vaibility\ (\%) = \frac{Absobance\ of\ treated\ cells - Absorbance\ of\ media}{Absorbance\ of\ negative\ control\ cells - Absorbance\ of\ media} \times 100$$

4.7 Assessment of ROS generated by laser irradiation in vitro

ROS generation was evaluated in vitro using Singlet Oxygen Sensor Green (SOSG; Thermo Fisher Scientific, USA). Briefly, 100 μL of either MOF525 or R848@MOF525 suspended in medium (25 μg/mL) was added in black 96-well plates. Subsequently, 100 μL of 10 μM SOSG dissolved in medium was added to the wells and mixed via pipetting. The resulting mixture was irradiated with a 660 nm laser (500 mW, 10 min). The SOSG intensity at each timepoint was measured using a microplate reader at 500 nm with a reference wavelength at 530 nm.

4.8 Assessment of PDT-induced cytotoxicity in vitro

PDT-induced cytotoxicity of MOF525 and R848@MOF525 was assessed using CT26 cells. Cells were seeded at a density of 1.0×10^4 cells/well in a 96-well cell culture plate. After 24 h, the medium was removed and replaced with medium with either MOF525 (50 μg/mL) or R848@MOF525 (50 μg/mL). Cells were irradiated with a 660 nm laser (500 mW) for 5 min, rested for 1 min, then re-irradiated for 5 min (total 10 min irradiation) After 24 h, cell viability was evaluated using EZ-Cytox, as described above.

4.9 Assessment of ATP release in vitro

ATP released after MOF525 treatment and laser irradiation was evaluated using a commercial PicoSens^{TM} ATP Assay Kit (BIOMAX, Korea). CT26 cells were seeded at a density of 1×10^6 cells/well in a 24-well cell culture plate and incubated for 24 h. The cells were treated with MOF525 (50 μg/mL) dispersed in medium, then irradiated with a 660 nm laser (500 mW) for 10 min (5 min irradiation, 1 min rest, 5 min irradiation). After 24 h, ATP measurement was performed according to the instructions provided by the manufacturer.

4.10 Assessment of photothermal properties of MOF525

Temperatures changes of MOF525 following laser irradiation was evaluated using a thermal imaging camera (MobIR Air, GUIDE, China). Either MOF525 (50 μg/mL) or PBS in 1.5 mL centrifuge tubes were irradiated with a 660 nm laser (500 mW) for 5 min. Solution temperatures were measured and recorded at predetermined time points (0, 1, 2, 3, 4, 5 min).

4.11 Culture of Bone marrow-derived dendritic cells (BMDCs)

Mouse bone marrow progenitor cells were isolated and differentiated to dendritic cells following a previous study with slight modifications [74]. In brief, bone marrow progenitor cells were flushed from the femurs and tibias of BALB/c mice using a syringe. After removing red blood cells with ACK Lysing Buffer (Gibco, USA), purified bone marrow cells were cultured in 100 mm petri dishes using RPMI with 20 ng/mL of granulocyte-macrophage colony-stimulating factor (GM-CSF, Biolegend, USA). On day 6, non-adherent and loosely adherent cell clusters were considered as proliferating immature DCs and were harvested using 2 mM ethylene-diamine-tetraacetic acid (EDTA) and used accordingly.

4.12 In vitro stimulation of BMDCs

BMDCs were seeded in non-treated 96-well cell culture plates at 1.0×10^5 cells/well and treated with either MOF525 (50, 25, and 10 μg/mL) or R848@MOF525 (50, 25, and 10 μg/mL). LPS (100 ng/mL) or R848 (2 μg/mL) was used as a positive control for BMDC activation. After 24 h, expression of BMDC activation markers were evaluated using a flow cytometer (Cytoflex, Beckman Coulter, USA). The following antibodies were used in this study: Zombie Violet™ Viability Dye, CD11c (PerCP-Cy5.5), CD86 (PE), and MHCII (FITC) (Biolegend, USA).

4.13 Animals

All animal experiments were conducted in accordance with the protocols approved by the Institutional Animal Care and Use Committee (IACUC) of Sungkyunkwan University College of Medicine (IACUC No. SKKU IACUC 2024-02-40-1). BALB/c mice (female, 7 weeks old) were purchased from Orient Bio (Seongnam, Korea). All animals were housed under a 12:12 light–dark cycle and acclimatized for 7 days before any experiments.

4.14 Evaluation of in vivo antitumor efficacy

The antitumor efficacy of R848@MOF525 treatment was evaluated using a subcutaneous CT26 tumor model resembling CRC. BALB/c mice were subcutaneously inoculated with 5×10^5 CT26 cells suspended in 100 μL of PBS in the right flank. Tumor sizes were measured using a digital caliper and volumes were calculated using the following formula: $[\mathrm{Length} \times \mathrm{Width}^2 \times 0.5]$. Once tumor volumes reached approximately 100 mm^3, mice were randomly divided into one of the following treatment groups: PBS (100 μL), R848 (100 μL, 0.2 mg/mL in PBS), MOF525 (100 μL, 1 mg/mL in PBS), R848@MOF525 (100 μL, 1 mg/mL in PBS), MOF525 (100 μL, 1 mg/mL in PBS) + Laser, or R848@MOF525 (100 μL, 1 mg/mL in PBS) + Laser. Groups including laser treatment were irradiated with a 660 nm laser (500 mW) for a total of 10 min (5 min irradiation, 1 min rest, 5 min irradiation). Treatments were provided as either 3-day intervals (Day 16, Day 19, Day 22, Day 25 post-inoculation) or 5-day intervals (Day 13, Day 18, Day 23, Day 28 post-inoculation). Tumor sizes and body weights were measured after each treatment. Tumor tissues from PBS, R848, MOF525 and R848@MOF525 treatment groups were extracted 40 days post-inoculation for histopathological evaluations. Since MOF525 + Laser and R848@MOF525 + Laser groups exhibited complete tumor regression, a tumor re-challenge test was conducted instead at Day 60 post-inoculation. For tumor re-challenge tests, cell volumes identical to those of the primary inoculation was injected to the opposite flank and tumor growth was monitored for 3 additional weeks. Vital organs from these mice were then extracted for biosafety evaluations. All procedures, including tumor inoculation, were performed under isoflurane inhalation anesthesia.

4.15 Histopathological analysis

Both tumor samples and vital organs were collected and stored in 10% neutralized buffered formalin prior to histological analyses. Samples were embedded in paraffin blocks and sectioned (4 μm thickness) for either Hematoxylin and Eosin (H&E) staining or TUNEL staining. Images of H&E stained samples were obtained using an inverted light microscope (Amscope, USA), and quantitative analysis of tumor size and necrotic lesions was performed using the ImageJ software. TUNEL staining was performed according to the manufacturer's guidelines (Abcam, USA). In brief, slides were deparaffinized/hydrated, removed of endogenous peroxidase using H_2O_2 in methanol, then treated for pressurized heat antigen

retrieval in citrate buffer prior to staining. TUNEL staining images were obtained using an inverted light microscopy, evaluated using the ImageJ software.

4.16 Statistical analysis

Statistical analyses were performed using the GraphPad Prism 8 software (GraphPad Software, USA). Data are presented as mean ± standard deviation unless stated otherwise. The precise number of replicates or samples for each data is specified in the figure legend. Statistical significance between groups was assessed using one-way ANOVA followed by Tukey's post hoc multiple comparison test unless stated otherwise. P-values of $^{*}p < 0.0332$, $^{**}p < 0.0021$, $^{***}p < 0.0002$, and $^{****}p < 0.0001$ were considered statistically significant.

Supplementary Information

The online version contains supplementary material available at https://doi.org/10.1186/s40580-026-00544-2.

Supplementary Material 1

Acknowledgements
We extend our gratitude to the other contributors to this work.

Author contributions
N.K.L., S.-N.K., and C.G.P. designed the research; N.K.L., C.-P.J.W., S.-H.L., N.Y.C., Y.J.O., U.B., M.-S.K., and W.J. performed the experiment; N.K.L., C.-P.J.W., S.-N.K., and H.-J.K. analyzed the data; N.K.L. and C.-P.J.W. wrote the paper; T.-E.P., W.P., S.-N.K., and C.G.P. provided feedbacks and revised the paper.

Funding
This research was partly supported by the Institute of Information & Communications Technology Planning & Evaluation(IITP)-ITRC(Information Technology Research Center) grant funded by the Ministry of Science and ICT (MSIT) of the Republic of Korea (IITP-2026-RS-2023-00258971, 10%). This work was also supported and grant funded by the Korea University Guro Hospital (KOREA RESEARCH-DRIVEN HOSPITAL) and Korea University (K2505291). Additionally, this work was supported by the National Research Foundation of Korea grant funded by the MSIT (RS-2023-00208913, RS-2024-00440714, RS-2025-25424498). Finally, this research was supported by the Bio&Medical Technology Development Program of the National Research Foundation funded by the MSIT (RS-2024-00508402) and the Technology Development Program (RS-2024-00460563) funded by the Ministry of SMEs and Startups (MSS, Korea).

Data availability
All data generated or analyzed during this study are included in this published article and its supplementary information files.

Declarations

Ethics approval and consent to participate
This research received approval from the Ethics Committee of Sungkyunkwan University, and all procedures regarding animal studies followed established ethical standards approved by the Institutional Animal Care and Use Committee (IACUC) of Sungkyunkwan University College of Medicine (IACUC No.: SKKU IACUC 2024-02-40-1).

Consent for publication
Not applicable.

Competing interests
The authors Se-Na Kim, Nea Young Chun and Yu Jin Oh declare that patent applications related to the materials and methods described in this work have been filed in South Korea (Application No. 10-2023-0179991) and under the Patent Cooperation Treaty (PCT/KR2023/020618).

Author details
[1]Department of Intelligent Precision Healthcare Convergence, Institute for Cross- disciplinary Studies (ICS), Sungkyunkwan University (SKKU), Suwon, Gyeonggi 16419, Republic of Korea
[2]Department of Biomedical Engineering, ICS, SKKU, Suwon, Gyeonggi 16419, Republic of Korea
[3]Research and Development Center, MediArk Inc, Cheongju, Chungbuk 28644, Republic of Korea
[4]College of Pharmacy, Korea University, Sejong 30019, Republic of Korea
[5]Department of Biomedical Engineering, College of Information-Bio Convergence Engineering, Ulsan National Institute of Science and Technology, Ulsan 44919, Republic of Korea
[6]Department of Integrative Biotechnology, College of Biotechnology and Bioengineering, SKKU, Suwon, Gyeonggi 16419, Republic of Korea
[7]Department of MetaBioHealth, SKKU Institute for Convergence, SKKU, Suwon, Gyeonggi 16419, Republic of Korea
[8]Department of Industrial Cosmetic Science, Chungbuk National University, Cheongju, Chungbuk 28644, Republic of Korea

Received: 13 March 2026 / Accepted: 29 March 2026
Published online: 21 April 2026

References

1. R. Tian et al., Se-Containing MOF Coated Dual-Fe-Atom Nanozymes With Multi-Enzyme Cascade Activities Protect Against Cerebral Ischemic Reperfusion Injury. Adv. Funct. Mater. **32**, 2204025 (2022). https://doi.org/10.1002/adfm.202204025
2. Z. Chen et al., Engineering Ultra-Small Cerium-Based Metal–Organic Frameworks Nanozymes for Efficient Antioxidative Treatment of Dry Eye Disease. Adv. Funct. Mater. **34**, 2307569 (2023). https://doi.org/10.1002/adfm.202307569
3. A. Wang et al., Biomedical Metal-Organic Framework Materials: Perspectives and Challenges. Adv. Funct. Mater. **34**, 2308589 (2024). https://doi.org/10.1002/adfm.202308589
4. Z. Yu et al., Enzyme-Encapsulated Protein Trap Engineered Metal–Organic Framework-Derived Biomineral Probes for Non-Invasive Prostate Cancer Surveillance. Adv. Funct. Mater. **33**, 2301457 (2023). https://doi.org/10.1002/adfm.202301457
5. T. Jia et al., Metalloporphyrin MOFs-Based Nanoagent Enabling Tumor Microenvironment Responsive Sonodynamic Therapy of Intracranial Glioma Signaled by NIR-IIb Luminescence Imaging. Adv. Funct. Mater. **34**, 2307816 (2023). https://doi.org/10.1002/adfm.202307816
6. S.R. Alves, I.R. Calori, A.C. Tedesco, Photosensitizer-based metal-organic frameworks for highly effective photodynamic therapy. Mater. Sci. Eng. C **131**, 112514 (2021). https://doi.org/10.1016/j.msec.2021.112514
7. M.G. Goesten, F. Kapteijn, J. Gascon, Fascinating chemistry or frustrating unpredictability: observations in crystal engineering of metal–organic frameworks. CrystEngComm. **15**, 9249 (2013). https://doi.org/10.1039/c3ce41241e
8. J. Hwang, A. Ejsmont, R. Freund, J. Goscianska, B.V. Schmidt, S. Wuttke, Controlling the morphology of metal–organic frameworks and porous carbon materials: Metal oxides as primary architecture-directing agents. Chem. Soc. Rev. **49**, 3348 (2020). https://doi.org/10.1039/c9cs00871c
9. N.W. Ockwig, O. Delgado-Friedrichs, M. O'Keeffe, O.M. Yaghi, Reticular chemistry: occurrence and taxonomy of nets and grammar for the design of frameworks. Acc. Chem. Res. **38**, 176 (2005). https://doi.org/10.1021/ar020022l
10. X. Gong, H. Noh, N.C. Gianneschi, O.K. Farha, Interrogating kinetic versus thermodynamic topologies of metal–organic frameworks via combined transmission electron microscopy and X-ray diffraction analysis. J. Am. Chem. Soc. **141**, 6146 (2019). https://doi.org/10.1021/jacs.9b01789
11. L. Yuan et al., A S-Scheme MOF-on-MOF Heterostructure. Adv. Funct. Mater. **33**, 2214627 (2023). https://doi.org/10.1002/adfm.202214627

12. E. Ploetz, H. Engelke, U. Lächelt, S. Wuttke, The Chemistry of Reticular Framework Nanoparticles: MOF, ZIF, and COF Materials. Adv. Funct. Mater. **30**, 1909062 (2020). https://doi.org/10.1002/adfm.201909062
13. H. Li, K. Wang, Y. Sun, C.T. Lollar, J. Li, H.-C. Zhou, Recent advances in gas storage and separation using metal–organic frameworks. Mater. Today. **21**, 108 (2018). https://doi.org/10.1016/j.mattod.2017.07.006
14. H. Furukawa et al., Ultrahigh porosity in metal-organic frameworks. Science. **329**, 424 (2010). https://doi.org/10.1126/science.1192160
15. K. Yu, Y.R. Lee, J.Y. Seo, K.Y. Baek, Y.M. Chung, W.S. Ahn, Sonochemical synthesis of Zr-based porphyrinic MOF-525 and MOF-545: Enhancement in catalytic and adsorption properties. Microporous Mesoporous Mater. **316** (2021). https://doi.org/10.1016/j.micromeso.2021.110985
16. M. Lismont, L. Dreesen, S. Wuttke, Metal-Organic Framework Nanoparticles in Photodynamic Therapy: Current Status and Perspectives. Adv. Funct. Mater. **27**, 1606314 (2017). https://doi.org/10.1002/adfm.201606314
17. Z.H. Zhu et al., Nanoscale Metal-Organic Framework Leveraging Water, Oxygen, and Hydron Peroxide to Generate Reactive Oxygen Species for Cancer Therapy. Adv. Funct. Mater. **35**, 2419548 (2025). https://doi.org/10.1002/adfm.202419548
18. D.X. Xu, Q. Duan, H. Yu, W.Y. Dong, Photodynamic therapy based on porphyrin-based metal-organic frameworks. J. Mater. Chem. B **11**, 5976 (2023). https://doi.org/10.1039/d2tb02789e
19. J. Kou, D. Dou, L. Yang, Porphyrin photosensitizers in photodynamic therapy and its applications. Oncotarget. **8**, 81591 (2017). https://doi.org/10.18632/oncotarget.20189
20. A.P. Castano, P. Mroz, M.R. Hamblin, Photodynamic therapy and anti-tumour immunity. Nat. Rev. Cancer. **6**, 535 (2006). https://doi.org/10.1038/nrc1894
21. D. van Straten, V. Mashayekhi, H.S. de Bruijn, S. Oliveira, D.J. Robinson, Oncologic Photodynamic Therapy: Basic Principles, Current Clinical Status and Future Directions. Cancers (Basel). **9**, 19 (2017). https://doi.org/10.3390/cancers9020019
22. J.H. Correia, J.A. Rodrigues, S. Pimenta, T. Dong, Z. Yang, Photodynamic Therapy Review: Principles, Photosensitizers, Applications, and Future Directions. Pharmaceutics. **13**, 1332 (2021). https://doi.org/10.3390/pharmaceutics13091332
23. J.A. Rodrigues, J.H. Correia, Enhanced Photodynamic Therapy: A Review of Combined Energy Sources. Cells. **11**, 3995 (2022). https://doi.org/10.3390/cells11243995
24. C.W. Ng, J. Li, K. Pu, Recent Progresses in Phototherapy-Synergized Cancer Immunotherapy. Adv. Funct. Mater. **28**, 1804688 (2018). https://doi.org/10.1002/adfm.201804688
25. H. Wang, X. Han, Z. Dong, J. Xu, J. Wang, Z. Liu, Hyaluronidase with pH-responsive Dextran Modification as an Adjuvant Nanomedicine for Enhanced Photodynamic-Immunotherapy of Cancer. Adv. Funct. Mater. **29**, 1902440 (2019). https://doi.org/10.1002/adfm.201902440
26. Z. Zhang et al., Structural analyses of toll-like receptor 7 reveal detailed RNA sequence specificity and recognition mechanism of agonistic ligands. Cell. Rep. **25**, 3371 (2018). https://doi.org/10.1016/j.celrep.2018.11.081
27. A. Larange, D. Antonios, M. Pallardy, S. Kerdine-Römer, TLR7 and TLR8 agonists trigger different signaling pathways for human dendritic cell maturation. J. Leukoc. Biol. **85**, 673 (2009). https://doi.org/10.1189/jlb.0808504
28. J.K. Dowling, A. Mansell, Toll-like receptors: the swiss army knife of immunity and vaccine development. Clin. Transl Immunol. **5**, e85 (2016). https://doi.org/10.1038/cti.2016.22
29. T.H. Mogensen, Pathogen recognition and inflammatory signaling in innate immune defenses. Clin. Microbiol. Rev. **22**, 240 (2009). https://doi.org/10.1128/CMR.00046-08
30. S. Akira, H. Hemmi, Recognition of pathogen-associated molecular patterns by TLR family. Immunol. Lett. **85**, 85 (2003). https://doi.org/10.1016/s0165-2478(02)00228-6
31. A. Ozinsky et al., The repertoire for pattern recognition of pathogens by the innate immune system is defined by cooperation between toll-like receptors. Proc. Natl. Acad. Sci. U S A **97**, 13766 (2000). https://doi.org/10.1073/pnas.250476497
32. J. Hua et al., Current Strategies for Tumor Photodynamic Therapy Combined With Immunotherapy. Front. Oncol. **11**, 738323 (2021). https://doi.org/10.3389/fonc.2021.738323
33. Y. Zhang, Y. Liao, Q. Tang, J. Lin, P. Huang, Biomimetic Nanoemulsion for Synergistic Photodynamic-Immunotherapy Against Hypoxic Breast Tumor. Angew Chem. Int. Ed. Engl. **60**, 10647 (2021). https://doi.org/10.1002/anie.202015590
34. Q. Liu et al., Near-Infrared-II Nanoparticles for Cancer Imaging of Immune Checkpoint Programmed Death-Ligand 1 and Photodynamic/Immune Therapy. ACS Nano. **15**, 515 (2021). https://doi.org/10.1021/acsnano.0c05317
35. M. Chang et al., Colorectal Tumor Microenvironment-Activated Bio-Decomposable and Metabolizable Cu(2) O@CaCO(3) Nanocomposites for Synergistic Oncotherapy. Adv. Mater. **32**, e2004647 (2020). https://doi.org/10.1002/adma.202004647
36. N. Shang et al., Dendritic cells based immunotherapy. Am. J. Cancer Res. **7**, 2091 (2017)
37. X. Duan, C. Chan, W. Lin, Nanoparticle-Mediated Immunogenic Cell Death Enables and Potentiates Cancer Immunotherapy. Angew Chem. Int. Ed. Engl. **58**, 670 (2019). https://doi.org/10.1002/anie.201804882
38. L. Galluzzi, A. Buque, O. Kepp, L. Zitvogel, G. Kroemer, Immunogenic cell death in cancer and infectious disease. Nat. Rev. Immunol. **17**, 97 (2017). https://doi.org/10.1038/nri.2016.107
39. R. Falk-Mahapatra, S.O. Gollnick, Photodynamic therapy and immunity: an update. Photochem. Photobiol. **96**, 550 (2020). https://doi.org/10.1111/php.13253
40. P.C. Kousis, B.W. Henderson, P.G. Maier, S.O. Gollnick, Photodynamic therapy enhancement of antitumor immunity is regulated by neutrophils. Cancer Res. **67**, 10501 (2007). https://doi.org/10.1158/0008-5472.Can-07-1778
41. J. Liu et al., Co-delivery of IOX1 and doxorubicin for antibody-independent cancer chemo-immunotherapy. Nat. Commun. **12**, 2425 (2021). https://doi.org/10.1038/s41467-021-22407-6
42. J. Lou, L. Zhang, G. Zheng, Advancing cancer immunotherapies with nanotechnology. Adv. Ther. **2**, 1800128 (2019). https://doi.org/10.1002/adtp.201800128
43. C. Tang et al., Porphyrin-Based Metal-Organic Framework Materials: Design, Construction, and Application in the Field of Photocatalysis. Molecules. **29**, 467 (2024). https://doi.org/10.3390/molecules29020467
44. Z. Wang et al., Recent advances in porphyrin-based MOFs for cancer therapy and diagnosis therapy. Coord. Chem. Rev. **439**, 213945 (2021). https://doi.org/10.1016/j.ccr.2021.213945
45. G.G. Matlou, H. Abrahamse, Nanoscale metal-organic frameworks as photosensitizers and nanocarriers in photodynamic therapy. Front. Chem. **10**, 971747 (2022). https://doi.org/10.3389/fchem.2022.971747
46. K. Yu, D.I. Won, W.I. Lee, W.S. Ahn, Porphyrinic zirconium metal-organic frameworks: Synthesis and applications for adsorption/catalysis. Korean J. Chem. Eng. **38**, 653 (2021). https://doi.org/10.1007/s11814-020-0730-z
47. Y.Y. Liu, L.J. Chen, X. Zhao, X.P. Yan, Effect of Topology on Photodynamic Sterilization of Porphyrinic Metal-Organic Frameworks. Chemistry. **27**, 10151 (2021). https://doi.org/10.1002/chem.202100920
48. W. Morris et al., Synthesis, Structure, and Metalation of Two New Highly Porous Zirconium Metal–Organic Frameworks. Inorg. Chem. **51**, 6443 (2012). https://doi.org/10.1021/ic300825s
49. H.H. Yuan et al., Regulating Tumor-Associated Macrophage Polarization by Cyclodextrin-Modified PLGA Nanoparticles Loaded with R848 for Treating Colon Cancer. Int. J. Nanomed. **19** (2024). https://doi.org/10.2147/IJN.S450205
50. T.H. Chang et al., Planar Heterojunction Perovskite Solar Cells Incorporating Metal-Organic Framework Nanocrystals. Adv. Mater. **27**, 7229 (2015). https://doi.org/10.1002/adma.201502537
51. K.A.-O. Hadjiivanov et al., Power of Infrared and Raman Spectroscopies to Characterize Metal-Organic Frameworks and Investigate Their Interaction with Guest Molecules. Chem. Rev. **121**, 1286 (2020). https://doi.org/10.1021/acs.chemrev.0c00487
52. Y. Yuan et al., Zirconium nitride catalysts surpass platinum for oxygen reduction. Nat. Mater. **19**, 282 (2020). https://doi.org/10.1038/s41563-019-0535-9
53. H.B. Ji et al., Metal-organic framework for biomimetic nitric oxide generation and anticancer drug delivery. Biomater. Adv. **145**, 213268 (2023). https://doi.org/10.1016/j.bioadv.2022.213268
54. H. Su, S. Lv, H. Song, K. Shi, J. Zhu, Y. Zhang, Recent advances in continuous zirconium-based metal–organic framework membranes for high-precision separation. Sep. Purif. Technol. **345** (2024). https://doi.org/10.1016/j.seppur.2024.127318
55. S. Gruber, A. Nickel, Toxic or not toxic? The specifications of the standard ISO 10993-5 are not explicit enough to yield comparable results in the cytotoxicity assessment of an identical medical device. Front. Med. Technol. **5**, 1195529 (2023). https://doi.org/10.3389/fmedt.2023.1195529
56. O. Jung et al., Improved In Vitro Test Procedure for Full Assessment of the Cytocompatibility of Degradable Magnesium Based on ISO 10993-5/-12. Int. J. Mol. Sci. **20** (2019). https://doi.org/10.3390/ijms20020255

57. M. Payne, S.H. Bossmann, M.T. Basel, Direct treatment versus indirect: Thermoablative and mild hyperthermia effects. Wiley Interdiscip Rev. Nanomed. Nanobiotechnol. **12**, e1638 (2020). https://doi.org/10.1002/wnan.1638
58. Y. Reissis, E. Garcia-Gareta, M. Korda, G.W. Blunn, J. Hua, The effect of temperature on the viability of human mesenchymal stem cells. Stem Cell. Res. Ther. **4**, 139 (2013). https://doi.org/10.1186/scrt350
59. W. Zhu et al., The role of hyperthermia in the treatment of tumor. Crit. Rev. Oncol. Hematol. **204**, 104541 (2024). https://doi.org/10.1016/j.critrevonc.2024.104541
60. V. Bosteels, S. Janssens, Striking a balance: new perspectives on homeostatic dendritic cell maturation. Nat. Rev. Immunol. **25**, 125 (2025). https://doi.org/10.1038/s41577-024-01079-5
61. R. Kim, M. Emi, K. Tanabe, Functional roles of immature dendritic cells in impaired immunity of solid tumour and their targeted strategies for provoking tumour immunity. Clin. Exp. Immunol. **146**, 189 (2006). https://doi.org/10.1111/j.1365-2249.2006.03215.x
62. S. Andreae, F. Piras, N. Burdin, F. Triebel, Maturation and activation of dendritic cells induced by lymphocyte activation gene-3 (CD223). J. Immunol. **168**, 3874 (2002). https://doi.org/10.4049/jimmunol.168.8.3874
63. C. Zhao, W. Song, J. Wang, X. Tang, Z. Jiang, Immunoadjuvant-functionalized metal-organic frameworks: synthesis and applications in tumor immune modulation. Chem Commun (Camb) 61, 1962 (2025). https://doi.org/10.1039/d4cc06510g
64. V.D. Ramanathan, P. Badenoch-Jones, J.L. Turk, Complement activation by aluminium and zirconium compounds. Immunology. **37**, 881 (1979)
65. S. Shima et al., IgM antibody production in mice intraperitoneally injected with zirconium oxychloride. Br. J. Ind. Med. **44**, 633 (1987). https://doi.org/10.1136/oem.44.9.633
66. J.O. Naim, C.J. van Oss, W. Wu, R.F. Giese, P.A. Nickerson, Mechanisms of adjuvancy: I–Metal oxides as adjuvants. Vaccine. **15**, 1183 (1997). https://doi.org/10.1016/s0264-410x(97)00016-9
67. C.B. Rodell et al., TLR7/8-agonist-loaded nanoparticles promote the polarization of tumour-associated macrophages to enhance cancer immunotherapy. Nat. Biomed. Eng. **2**, 578 (2018). https://doi.org/10.1038/s41551-018-0236-8
68. M.M. Alam, D. Yang, A. Trivett, T.J. Meyer, J.J. Oppenheim, HMGN1 and R848 Synergistically Activate Dendritic Cells Using Multiple Signaling Pathways. Front. Immunol. **9** (2018). https://doi.org/10.3389/fimmu.2018.02982
69. S. Schüller et al., The TLR-specific adjuvants R-848 and CpG-B endorse the immunological reaction of neonatal antigen-presenting cells. Pediatr. Res. **80**, 311 (2016). https://doi.org/10.1038/pr.2016.71
70. Y.L. Wang et al., Long-term relapse-free survival enabled by integrating targeted antibacteria in antitumor treatment. Nat. Commun. **15** (2024). https://doi.org/10.1038/s41467-024-48662-x
71. C. Liu et al., Systemic reprogramming of tumour immunity via IL-10-mRNA nanoparticles. Nat. Nanotechnol. **20**, 1526 (2025). https://doi.org/10.1038/s41565-025-01980-7
72. D.H. Nguyen et al., Reprogramming the tumor immune microenvironment using engineered dual-drug loaded Salmonella. Nat. Commun. **16** (2025). https://doi.org/10.1038/s41467-025-56044-0
73. C. Koschnick, M.W. Terban, S. Canossa, M. Etter, R.E. Dinnebier, B.V. Lotsch, Influence of Water Content on Speciation and Phase Formation in Zr-Porphyrin-Based MOFs. Adv. Mater. **36**, e2210613 (2024). https://doi.org/10.1002/adma.202210613
74. J.H. Han et al., Image-guided cancer vaccination with combination of multifunctional nano-adjuvant and an irreversible electroporation technique. Biomaterials. **289** (2022). https://doi.org/10.1016/j.biomaterials.2022.121762

Publisher's note